

Article

Ba-mediated Pt/TiO₂ for Enhanced Low Temperature HCHO Oxidation Originated from the Interaction between Pt and Ba

Chenxuanzhi Ruan^{1,2}, Hongguo Gao¹, Xuejuan Zhao², Zelin Hua¹, Shenjie Lv¹, Shanshan Chen^{3,*}, and Licheng Li^{1,*}

¹ Jiangsu Co-Innovation Center of Efficient Processing and Utilization of Forest Resources, College of Chemical Engineering, Nanjing Forestry University, Nanjing 210037, China

² School of Materials Science and Engineering, Nanjing Institute of Technology, Nanjing 211167, China

³ School of Materials Science and Engineering, Nankai University, Tianjin 300350, China

* Correspondence: sschen@nankai.edu.cn (S.C.); lilc@njfu.edu.cn (L.L.)

Received: 22 January 2025; Revised: 27 February 2025; Accepted: 10 March 2025; Published: 11 March 2025

Abstract: The alkaline earth metals have recently been reported to exhibit a similar role as alkali metals in enhancing the low temperature formaldehyde (HCHO) oxidation performance of precious metal supported catalysts; however, its essential mechanism is still not well understood. In this work, it is found that the Pt precursor is critical for Ba-mediated Pt/TiO₂ catalyst to achieve the efficient HCHO oxidation performance. Catalytic results indicate that Pt/TiO₂ catalysts using tetraammineplatinum(II) nitrate (Pt(NH₃)₄(NO₃)₂) and chloroplatinic acid (H₂PtCl₆) as Pt precursors exhibit comparable performance in HCHO oxidation. Notably, the Ba-mediated Pt/TiO₂ catalyst synthesized from Pt(NH₃)₄(NO₃)₂ shows exceptional catalytic performance, with its HCHO reaction rate being 3.8-fold that of Pt/TiO₂, while the Ba-mediated Pt/TiO₂ catalyst derived from H₂PtCl₆ has the similar catalytic activity to that of Pt/TiO₂. Series characterization results reveal that the Ba species can strongly interact with Pt to form the Ba-O-Pt active site within the Ba-mediated Pt/TiO₂ catalyst derived from Pt(NH₃)₄(NO₃)₂. However, such interaction is not observed in the catalyst synthesized from H₂PtCl₆. Additionally, more oxygen species and hydroxyl groups can be adsorbed and activated on the Ba-O-Pt active site than those on the typical Pt active site, and HCHO undergoes efficient oxidation on the Ba-O-Pt active site via a different reaction pathway (HCHO → HCOO⁻ + OH → H₂O + CO₂) analogous to that observed on alkali metal-mediated active site. These findings can provide a deep insight into the development of highly efficient catalysts for low temperature HCHO oxidation.

Keywords: barium; platinum precursor; formaldehyde; catalytic oxidation; active site

1. Introduction

Formaldehyde (HCHO) is a prevalent indoor air pollutant, classified as a Group I carcinogen by the international agency for research on cancer. Various technologies, such as biological purification, adsorption, photocatalysis, and catalytic oxidation, are commonly utilized to mitigate indoor HCHO pollution. Among them, low temperature catalytic oxidation has been widely demonstrated as a viable approach for HCHO removal [1,2]. Compared to other types of catalysts, the supported precious metal catalysts, especially for Pt, have the superior catalytic activity for HCHO oxidation at room temperature [1,3,4]. Nevertheless, given the high cost of precious metals and the irreplaceable advantages of HCHO oxidation, there is a strong rationale for the development of highly efficient precious metal catalysts to alleviate their associated expenses.

Over the past few decades, a variety of strategies, including the selection of appropriate supports, enhancement of adsorption capabilities, and incorporation of promoter, have been developed to modulate the catalytic performance of HCHO oxidation catalysts [4–6]. By comparison, the introduction of promoter is considered as a viable and convenient approach due to its enhanced technical and economic features as well as ease of implementation. Notably, alkali metals are one type of the most effective promoters for significantly enhancing the catalytic HCHO oxidation performance of the precious metal catalysts. He et al. firstly investigated the mechanism of alkali metal (e.g., Li, Na, K and Cs) and found that the introduction of alkali metal ions could



Copyright: © 2025 by the authors. This is an open access article under the terms and conditions of the Creative Commons Attribution (CC BY) license (<https://creativecommons.org/licenses/by/4.0/>).

Publisher's Note: Scilight stays neutral with regard to jurisdictional claims in published maps and institutional affiliations.

induce and stabilize the dispersed Pt species to form a new type of active site, i.e., alkali metal-O-Pt. More importantly, the adsorbed hydroxyl could be activated on these active sites to react with formate into CO₂ and H₂O, thus opening a more efficient reaction pathway of HCHO oxidation [7,8]. Subsequently, the preparation parameters of alkali metal-mediated catalysts, including the types of precursor and support, the loading amount of metals and promoters, were found to be sensitive to the catalytic HCHO oxidation performance of the catalysts [9–11]. Up to date, the promotion role of alkali metals in the oxidation catalysts for HCHO has been mostly elucidated, and their optimal preparation methods have been well established.

By comparison, alkali earth metals are relatively less applied in the catalytic HCHO oxidation. Further investigation is needed to determine whether they exhibit similar promoting effects in HCHO oxidation as neighboring alkali metals. Actually, extensive research in other reactions has been reported that the presence of alkaline earth metals can facilitate the catalytic reactions, such as water-gas shift, alkene transfer hydrogenation, NO reduction, methane combustion and toluene steam reforming [12–17]. Depending on the specific catalytic reactions under consideration, alkali earth metals have the potential to serve as chemical promoters by influencing the electron density at the metal-support interface or altering the chemical adsorption properties of the dispersed metals and their interaction with precious metals [12,17,18]. Moreover, they can also function as the structural promoters by enhancing the dispersion of the active sites or stabilizing the dispersed metal species from being sintered [16,19,20]. It is the water-gas shift reaction that has been inspired based on the applied catalysts for the extension application of HCHO oxidation reaction [7,21]. The preliminary investigation indicated that the incorporation of alkaline earth metals as promoters could yield a similar effect to that of alkali metals in enhancing the catalytic performance of HCHO oxidation [22]. However, the corresponding insight into the promotion roles is still not well understood, which is critical to the development of alkali metals mediated catalysts for efficient low temperature HCHO oxidation.

Based on the aforementioned considerations, by taking the Ba-mediated Pt/TiO₂ catalyst as a prototype, the roles of the Pt precursor for the catalyst preparation in affecting the HCHO oxidation performance has been elucidated in this work. Considering the presence of Pt in both cationic and anionic forms within the precursor, H₂PtCl₆ and Pt(NH₃)₄(NO₃)₂ were selected as the subjects of this research. Herein, the detailed preparation process of Ba-mediated Pt/TiO₂ is optimized in accordance with the catalytic performance. Moreover, a comprehensive analysis of the structures of Ba-mediated Pt/TiO₂ at various preparation stages is conducted using series characterization techniques, with the aim to understand why the different Pt precursors can significantly influence the catalytic performance. By integrating reaction kinetics and in situ spectroscopy studies, the corresponding work mechanism of Ba-mediated Pt/TiO₂ catalyst is elucidated and provided.

2. Experimental

2.1. Materials and Synthesis

Tetraammineplatinum(II) nitrate (Pt(NH₃)₄(NO₃)₂, Shanghai Macklin Biochemical Technology Co., Ltd., Shanghai, China), chloroplatinic acid (H₂PtCl₆·6H₂O, Shanghai Agent Co., Ltd., Shanghai, China), commercial titanium dioxide (TiO₂, Degussa, Frankfurt, Germany), barium nitrate (Ba(NO₃)₂, Nanjing Chemical Reagent Co., Ltd., Nanjing, China) were used as received.

The loading of Pt and Ba onto TiO₂ was achieved through a conventional co-impregnation method. Specifically, the dried TiO₂ powder was uniformly dispersed in an aqueous solution containing Pt precursors and Ba(NO₃)₂ with a Pt loading amount of 1 wt.%. Following drying at 105 °C for 12 h, the impregnated powder was calcined at 500 °C for 2 h. Subsequently, the calcined powder was reduced in H₂ at 300 °C for 2 h to obtain the Ba-mediated Pt/TiO₂ catalyst. The Ba-mediated Pt/TiO₂ catalysts prepared using H₂PtCl₆ and Pt(NH₃)₄(NO₃)₂ as Pt precursors were designated as Ba-Pt/TiO₂(H₂PtCl₆) and Ba-Pt/TiO₂(Pt(NH₃)₄(NO₃)₂), respectively. For comparison, the Pt/TiO₂ catalysts were prepared by impregnating Pt precursors of H₂PtCl₆ and Pt(NH₃)₄(NO₃)₂, and other preparation steps were identical to those of Ba-mediated Pt/TiO₂. These obtained catalysts were denoted as Pt/TiO₂(H₂PtCl₆) and Pt/TiO₂(Pt(NH₃)₄(NO₃)₂), respectively. Moreover, the synthesis of Ba/TiO₂ was conducted by the same impregnation method with an aqueous solution of Ba(NO₃)₂ followed by the same high temperature calcination treatment.

2.2. Characterization

The X-ray diffraction (XRD) patterns of the samples were obtained using a Rigaku Ultima IV X-ray diffractometer (Rigaku, Tokyo, Japan) at a scanning rate of 10°·min⁻¹ and a step size of 0.02°. The surface area (S_{BET}), pore volume (V_P), and pore size distribution of the samples were determined by the Brunner-Emmet-Teller

(BET) method, nitrogen adsorption at a relative pressure of 0.99, and the Barret-Joyner-Halenda (BJH) method, respectively. These experiments were performed on an ASAP 2020 system (Micromeritics, Norcross, GA, USA). A JEM-2100Plus transmission electron microscopy (TEM, Jeol, Tokyo, Japan) operating at 200 kV was employed to investigate the nanoscale morphology of the samples. The chemical valence states of Pt, Ba, Ti, and O species were characterized using an AXIS UltraDLD X-ray photoelectron spectroscopy (XPS, Shimadzu, Kyoto, Japan) with a monochromatic Al K α X-ray source. The binding energies of all elements were referenced to the C 1s peak at 284.6 eV. The absorption spectrum of the sample in the wavelength range from 250 to 800 nm was acquired at ambient temperature using a UV-2802 ultraviolet-visible spectrophotometer (Unico, Franksville, WI, USA).

Hydrogen temperature-programmed reduction (H₂-TPR) and oxygen temperature-programmed desorption (O₂-TPD) experiments were performed on the Micromeritics AutoChem II 2920 apparatus (Altamira Instrument, Cumming, GA, USA). For H₂-TPR, 100 mg of the catalyst was subjected to in-situ pretreatment at 400 °C for 30 min under 10% O₂/He atmosphere. After being cooled down, the sample was purged with 10% H₂/Ar gas at a flow rate of 30 mL·min⁻¹. The temperature was subsequently raised from -50 °C to 600 °C at a rate of 10 °C·min⁻¹ and the changes in the composition of the exhaust gas were recorded by a thermal conductivity detector (TCD). For O₂-TPD, 100 mg of the catalyst was initially in situ pretreated with 10% H₂/Ar gas at 300 °C for 30 min. Subsequently, the temperature was reduced to 0 °C, followed by switching the gas atmosphere to O₂ for adsorption. After 30 min, pure He gas was flowed for another 30 min to remove the weakly adsorbed O₂. Finally, the temperature was enhanced to 600 °C at a rate of 10 °C·min⁻¹, and the desorption signal of the exhaust gas was recorded synchronously.

The diffuse reflectance infrared Fourier transform spectroscopy (DRIFTS) experiment was performed using a Nicolet-6700 FTIR (Thermo Scientific, Waltham, MA, USA) spectrometer with a diffuse reflectance accessory and a mercury cadmium telluride (MCT) detector. Herein, DRIFTS tests contained HCHO-DRIFTS and CO-DRIFTS depending on different adsorbates. Initially, the HCHO-DRIFTS experiment was performed to investigate the reaction mechanism of HCHO oxidation on various catalysts. 100 mg of the catalyst was placed in the in-situ chamber, and then was pretreated in a pure N₂ flow of 30 mL·min⁻¹ from room temperature to 105 °C for 15 min at a rate of 10 °C·min⁻¹. After being cooling to 25 °C, the in-situ chamber was introduced by a HCHO/N₂ mixture flow of 30 mL·min⁻¹ with purging for 1 h, followed by switching to pure N₂ and pure O₂ for 0.5 h each to study the consumption and oxidation of different intermediates. The DRIFT spectra during these processes were recorded after 32 scans with a resolution of 4 cm⁻¹. Secondly, CO-DRIFTS experiment was conducted to analyze the dispersion state of Pt nanoparticles. The catalyst powder underwent the same pretreatment in the in-situ chamber as that of HCHO-DRIFTS experiment. Subsequently, pure CO gas was introduced into the in-situ chamber at a rate of 30 mL·min⁻¹ for 0.5 h. Finally, pure N₂ was used to purge the excess and weakly adsorbed CO in the in-situ chamber and the diffuse reflectance spectra were synchronously recorded based on the above requirements.

2.3. Catalytic Performance Evaluation

The HCHO oxidation reaction catalyzed by various catalysts was performed in a fixed bed flow reactor. During a typical run, 50 mg of the catalyst was placed in the constant temperature segment of the reactor. The feed gas containing 300 ppm HCHO, water vapor (relative humidity of ~5%), 20 vol.% O₂ and balanced N₂ was introduced into the reactor at the weight hourly space velocity (WHSV) of 52,000 h⁻¹. The HCHO conversion rates of the catalyst at different reaction temperatures were calculated based on the HCHO concentrations of the inlet (HCHO_{in}) and outlet (HCHO_{out}) gases according to the following equation.

$$\text{HCHO conversion rate (\%)} = \frac{\text{HCHO}_{\text{in}} - \text{HCHO}_{\text{out}}}{\text{HCHO}_{\text{in}}} \times 100$$

The long-term experiment of the catalyst was carried out on the above apparatus under the same reaction conditions. The HCHO conversion rate of the catalyst at room temperature was continuously monitored for 72 h to evaluate the catalytic stability of the catalyst. Moreover, the reaction kinetic experiments of various catalysts were conducted at the high WHSV of 90,000 h⁻¹ to remove the diffusion effect. The HCHO conversion rates at the reaction temperatures from 20 °C to 30 °C were obtained to calculate the intrinsic reaction rate and the activation energy (E_a) of the catalyst.

3. Results and Discussion

3.1. Catalytic Performance in HCHO Oxidation

The temperature-dependent HCHO conversion rates of various catalysts are depicted in Figure 1a. The Pt/TiO₂(H₂PtCl₆) catalyst exhibits a HCHO conversion rate of 20.0% at room temperature (25 °C), which increases with rising the reaction temperature, ultimately reaching 100.0% at 100 °C. This behavior aligns with the previously reported findings [23,24]. Similarly, the HCHO oxidation performance of Pt/TiO₂(Pt(NH₃)₄(NO₃)₂) has the comparable catalytic results to those of Pt/TiO₂(H₂PtCl₆). However, the Ba/TiO₂ and TiO₂ exhibit no HCHO conversion rate across all reaction temperatures. This result indicates that the Ba species does not contribute catalytically to the HCHO oxidation. Further investigation is carried out to check the impact of Ba species addition on the Pt/TiO₂ catalysts prepared from different Pt precursors. The result shows that the HCHO oxidation performance of the Ba-Pt/TiO₂(H₂PtCl₆) catalyst is similar to that of the corresponding Pt/TiO₂(H₂PtCl₆) catalyst. However, the Ba-Pt/TiO₂(Pt(NH₃)₄(NO₃)₂) catalyst has an enhanced HCHO oxidation performance that the conversion rate can reach up to 78.3% at room temperature, which exhibits a 3.8-fold increase in the intrinsic reaction rate compared to that of Pt/TiO₂(Pt(NH₃)₄(NO₃)₂). Additionally, the complete conversion of HCHO on Ba-Pt/TiO₂(Pt(NH₃)₄(NO₃)₂) is carried out at 60 °C. These results demonstrate that the precursor plays an important role in the achievement of highly active Ba-mediated Pt/TiO₂ catalysts.

Based on the Ba-Pt/TiO₂(Pt(NH₃)₄(NO₃)₂) catalyst, the effect of different Ba loadings on the HCHO oxidation performance is further examined. Figure 1b illustrates that there exists a volcano-type correlation between the Ba loading proportion and the HCHO conversion rate of the catalyst. When the Ba loading proportion is 2 wt.%, Ba-Pt/TiO₂(Pt(NH₃)₄(NO₃)₂) achieves the optimal performance. Therefore, subsequent investigations of the Ba-mediated Pt/TiO₂ catalyst are performed based on this optimized condition. The prolonged HCHO oxidation results of Pt/TiO₂(H₂PtCl₆), Ba-Pt/TiO₂(H₂PtCl₆), Pt/TiO₂(Pt(NH₃)₄(NO₃)₂) and Ba-Pt/TiO₂(Pt(NH₃)₄(NO₃)₂) catalysts are illustrated in Figure 1c. After continuous operation at room temperature for 72 h, it can be observed that the HCHO conversion rate of Ba-Pt/TiO₂(Pt(NH₃)₄(NO₃)₂) has experienced minimal loss. It demonstrates that the addition of Ba does not adversely affect the catalytic stability of the catalyst.

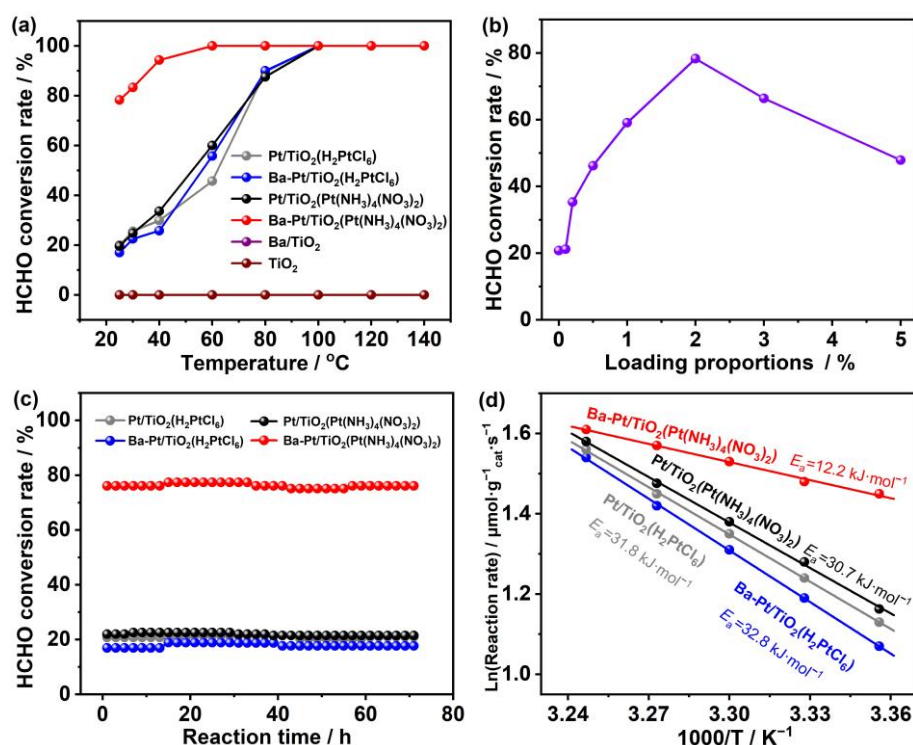


Figure 1. The temperature-dependent HCHO conversion rates of Pt/TiO₂(H₂PtCl₆), Ba-Pt/TiO₂(H₂PtCl₆), Pt/TiO₂(Pt(NH₃)₄(NO₃)₂), Ba-Pt/TiO₂(Pt(NH₃)₄(NO₃)₂), Ba/TiO₂ and TiO₂ catalysts (a) and various Pt/TiO₂(Pt(NH₃)₄(NO₃)₂) catalysts with different Ba loading proportions (b), long-term experimental (c) and reaction kinetic results (d) of various catalysts.

The results of reaction kinetics are displayed in Figure 1d. All four catalysts exhibit an excellent fit with the data ($R^2 > 0.998$), suggesting that the low temperature oxidation of HCHO on these catalysts obeys to the pseudo-first-order kinetic model [25,26]. Through calculations, the order of the activation energies (E_a) of four catalysts can be determined as follows: Ba-Pt/TiO₂(Pt(NH₃)₄(NO₃)₂) (12.2 kJ·mol⁻¹) < Pt/TiO₂(Pt(NH₃)₄(NO₃)₂) (30.7

$\text{kJ}\cdot\text{mol}^{-1}$) < Pt/TiO₂(H₂PtCl₆) (31.8 $\text{kJ}\cdot\text{mol}^{-1}$) < Ba-Pt/TiO₂(H₂PtCl₆) (32.8 $\text{kJ}\cdot\text{mol}^{-1}$). The general consensus is that the lower the E_a value, the more facile the oxidation of HCHO [27]. Thus, Ba-Pt/TiO₂(Pt(NH₃)₄(NO₃)₂) demonstrates the superior catalytic performance in HCHO oxidation, which aligns with the conclusion drawn from the aforementioned results. Furthermore, a comparative analysis of these four catalysts with the existing literature is conducted. As depicted in Table 1, Ba-Pt/TiO₂(Pt(NH₃)₄(NO₃)₂) catalyst exhibits the predominant feature in the activation energy and intrinsic reaction rate among the reported catalysts, demonstrating the significant promotion of Ba when it interacts with Pt/TiO₂ catalyst.

Table 1. Comparison of the catalytic performance for HCHO oxidation over various catalysts.

Catalyst	Loading Proportion (wt. %)		C ₀ (ppm)/GHSV (mL·h ⁻¹ ·g ⁻¹)	E _a (kJ·mol ⁻¹)	r _M ^a (μmol _{HCHO} ·g _{cat} ⁻¹ ·g ⁻¹)	Reference
	Metal	Promoter				
Pt/TiO ₂ (H ₂ PtCl ₆)	1.0	0	250/90,000	31.8	5.0	This work
Ba-Pt/TiO ₂ (H ₂ PtCl ₆)	1.0	2.0	250/90,000	32.8	4.3	This work
Pt/TiO ₂ (Pt(NH ₃) ₄ (NO ₃) ₂)	1.0	0	250/90,000	30.7	5.2	This work
Ba-Pt/TiO ₂ (Pt(NH ₃) ₄ (NO ₃) ₂)	1.0	2.0	250/90,000	12.2	19.6	This work
Na-Pt/TiO ₂	1.0	2.0	600/120,000	13 ± 4	-	[7]
Li-Pd/TiO ₂	1.0	1.0	140/190,000	-	2.8	[8]
Cs-Pd/TiO ₂	1.0	1.0	140/190,000	-	17.7	[8]
K-Pd/TiO ₂	1.0	1.0	550/640,000	-	1.8	[14]
Pd-Ba/TiO ₂	1.0	25.8	150/200,000	16.1	-	[22]
Pt/TiO ₂	1.0	0	400/80,000	-	4.8	[23]
Na-Pd/TiO ₂	1.0	2.0	140/190,000	-	2.2	[28]
K-Ag/Co ₃ O ₄	6.4	1.7	2000/165,000	28.5	0.037	[29]
K-Pt/NaY-2	0.08	15	300/100,000	12.0	0.0198	[30]

a: The intrinsic reaction rate was calculated from the kinetic experimental data at 25 °C.

3.2. Structural Properties of Catalyst

The XRD patterns of Pt/TiO₂(H₂PtCl₆), Ba-Pt/TiO₂(H₂PtCl₆), Pt/TiO₂(Pt(NH₃)₄(NO₃)₂) and Ba-Pt/TiO₂(Pt(NH₃)₄(NO₃)₂) samples are provided in Figure S1. All four catalysts exhibit five prominent diffraction peaks at 2θ of 25.4°, 37.8°, 49.7°, 53.9° and 55.1° in their patterns, corresponding to the characteristic peaks of anatase TiO₂. Moreover, there are three diffraction peaks at 27.5°, 36.1° and 41.2° that can be attributed to the rutile phase [31]. There is no diffraction peaks corresponding to the Ba species, e.g., BaTiO₃ or BaO [32,33], indicating that the Ba species is well dispersed in the Ba-Pt/TiO₂ catalysts. Similarly, the absence of platinum-related diffraction peaks in the XRD patterns also suggests that Pt nanoparticles exhibit in a high dispersion in four catalysts.

The N₂ adsorption-desorption isotherms and pore size distributions of various catalysts are displayed in Figure S2. All the isotherms exhibit type IV characteristics, suggesting that four catalysts possess mesoporous structure, as also demonstrated by the pore size distribution analyses. The detailed parameters of the pore structure are presented in Table S1. The surface area of Ba-Pt/TiO₂(Pt(NH₃)₄(NO₃)₂) (40.84 m²·g⁻¹) is slightly lower than that of Ba-Pt/TiO₂(H₂PtCl₆) (44.56 m²·g⁻¹), Pt/TiO₂(H₂PtCl₆) (46.87 m²·g⁻¹) and Pt/TiO₂(Pt(NH₃)₄(NO₃)₂) (41.78 m²·g⁻¹). Similarly, the pore volume of Ba-Pt/TiO₂(Pt(NH₃)₄(NO₃)₂) (0.23 cm³·g⁻¹) is marginally lower than those of Ba-Pt/TiO₂(H₂PtCl₆) (0.27 cm³·g⁻¹), Pt/TiO₂(H₂PtCl₆) (0.29 cm³·g⁻¹) and Pt/TiO₂(Pt(NH₃)₄(NO₃)₂) (0.24 cm³·g⁻¹), where this overall change is not significant. It indicates that the incorporation of Ba does not affect the pore structure of catalysts, which can be attributed to the good dispersion of the Ba species within Ba-mediated Pt/TiO₂. The similar parameters of pore structure of four catalysts suggest that the pore structure is not a primary factor in influencing the catalytic performance.

The nanostructure of the catalysts is characterized by TEM. As shown in Figure 2a,c,e,g, the morphology of TiO₂ support of four catalysts appears to be essentially identical. Figure 2b,d,f,h present the high-resolution TEM (HRTEM) images of the dark spots which are randomly selected from the left images for detailed analysis. The lattice fringe spacing is approximately 0.23 nm, which is ascribed to the Pt (111) plane of the metallic Pt [34]. Hence, these spots are identified as Pt nanoparticles. The statistical data inserted on the left side of Figure 2 reveals that the average Pt particle size of Ba-Pt/TiO₂(Pt(NH₃)₄(NO₃)₂) is 1.6 nm, which is much smaller than 2.5 nm, 2.4 nm and 2.4 nm of Pt/TiO₂(H₂PtCl₆), Ba-Pt/TiO₂(H₂PtCl₆), and Pt/TiO₂(Pt(NH₃)₄(NO₃)₂), respectively. This indicates that the addition of Ba, when using Pt(NH₃)₄(NO₃)₂ as the precursor, significantly enhances the dispersibility of Pt nanoparticles. Conversely, no such enhancement is observed when H₂PtCl₆ serves as the precursor. Then, we calculated the TOF value according to the dispersion degree to compare the difference among

those four catalysts. The TOF value for Ba-Pt/TiO₂(Pt(NH₃)₄(NO₃)₂) (5.6×10^{-4}) is much higher than those of Pt/TiO₂(H₂PtCl₆) (1.7×10^{-4}), Ba-Pt/TiO₂(H₂PtCl₆) (1.5×10^{-4}), and Pt/TiO₂(Pt(NH₃)₄(NO₃)₂) (1.7×10^{-4}). It means the intrinsic catalytic site of Ba-Pt/TiO₂(Pt(NH₃)₄(NO₃)₂) probably differs from the other three catalysts, leading to the remarkable promotion in the activity.

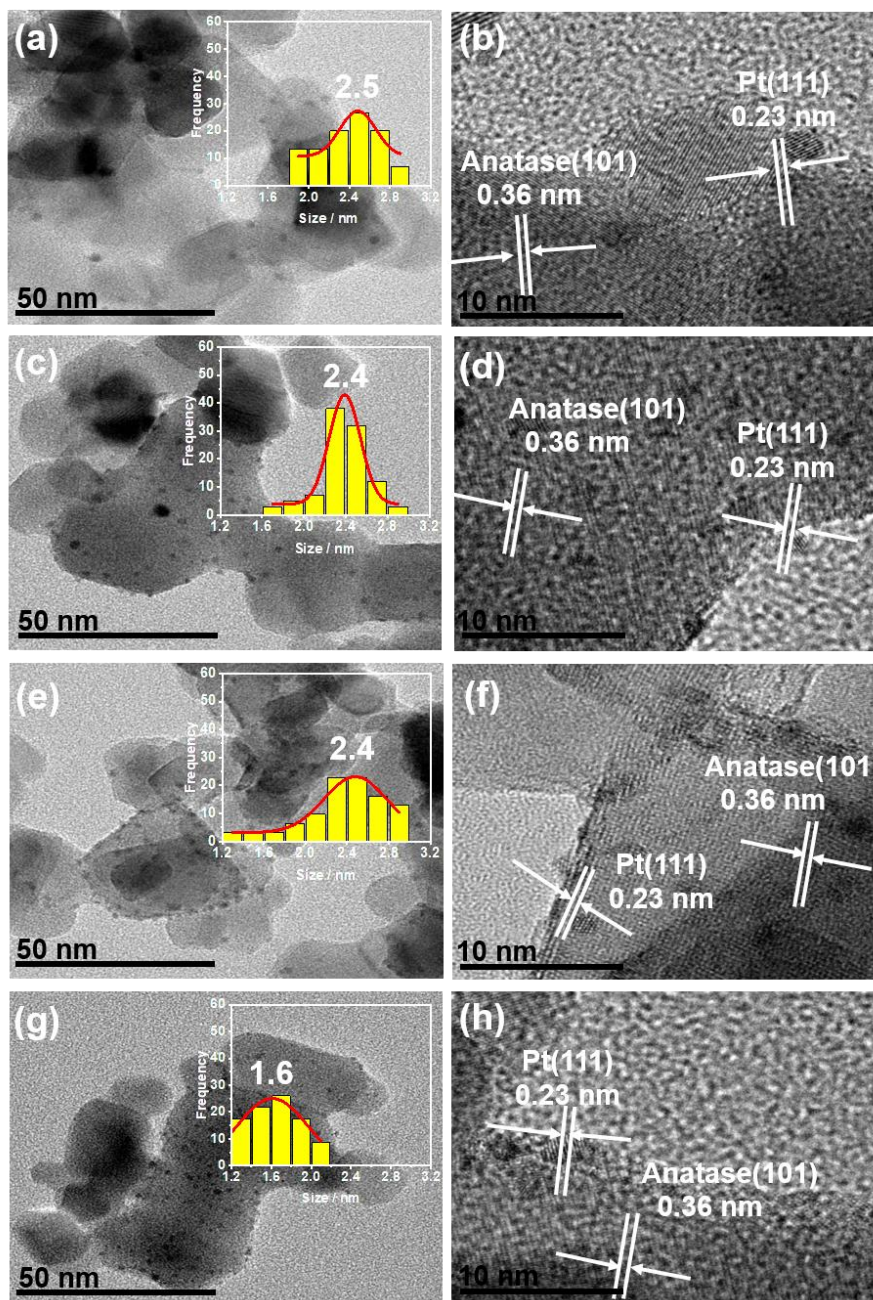


Figure 2. TEM and HRTEM images of Pt/TiO₂(H₂PtCl₆) (a,b), Ba-Pt/TiO₂(H₂PtCl₆) (c,d), Pt/TiO₂(Pt(NH₃)₄(NO₃)₂) (e,f) and Ba-Pt/TiO₂(Pt(NH₃)₄(NO₃)₂) (g,h) samples. Insets are the size distribution of Pt nanoparticles of the corresponding catalyst.

To conduct a more in-depth analysis of the detailed structure of Pt nanoparticles over four catalysts, the CO-DRIFTS experiment is carried out and the corresponding spectra are presented in Figure 3. Six distinct types of CO adsorption peaks are detected in the DRIFT spectra. The wavelength range observed within 2168 cm⁻¹ to 2170 cm⁻¹ pertains to gaseous CO, whereas the wavelength range observed within 2113 cm⁻¹ to 2122 cm⁻¹ corresponds to the adsorption of CO on single-atom Pt. Besides, the linearly adsorbed CO contains three bound types of CO to Pt terrace sites (2081~2089 cm⁻¹), step sites (2058~2066 cm⁻¹) and interface sites between Pt clusters and TiO₂ (2026~2033 cm⁻¹). Additionally, bridge bound CO is observed in the range of 1812~1835 cm⁻¹. Notably, it can be seen from the dynamic CO adsorption in situ DRIFTS (Figure S4) that by following N₂ purging, the CO adsorption peak at the single-atom site (2113 cm⁻¹) on Ba-Pt/TiO₂(Pt(NH₃)₄(NO₃)₂) exhibits a gradual decrease and can be

detected even after 30 min. It suggests Ba-Pt/TiO₂(Pt(NH₃)₄(NO₃)₂) possesses a notable affinity for CO adsorption at the single-atom Pt site. This phenomenon can be attributed to the stabilization of Pt nanoparticles by Ba species, which facilitates the formation of the Ba-O-Pt active site by reference to the methodology employed for determining the formation of alkali metal-mediated noble metal active site [7,9]. In addition, compared with the other three catalysts, Ba-Pt/TiO₂(Pt(NH₃)₄(NO₃)₂) exhibits lower frequencies in the spectral features of the step sites (2026 cm⁻¹), the interface sites between Pt clusters and the TiO₂ support (2058 cm⁻¹), and the bridge bound CO (1812 cm⁻¹). It is well established that the $\nu(\text{CO})$ vibration frequency is influenced by the strength of the C–O bond. The antibonding $2\pi^*$ –Pt interaction between CO and Pt involves an electron transfer from Pt to an antibonding orbital of CO. An increase in back-donation, which corresponds to a rise in the electron density within the $2\pi^*$ orbital of CO, results in a weakening of the C–O bond in CO molecules. This leads to a decrease in the $\nu(\text{CO})$ vibration frequency [14,35]. Therefore, the bridge bound CO peaks shift to lower wavenumbers as the electronegativity of alkaline earth metals decreases, indicating that the Pt species becomes more electron-rich. It further identifies the interaction between Pt and Ba in Ba-Pt/TiO₂(Pt(NH₃)₄(NO₃)₂) catalyst.

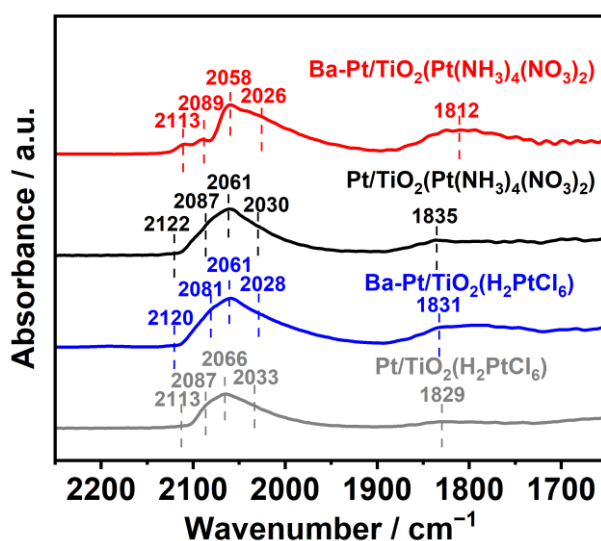


Figure 3. Stable CO-DRIFT spectra of Pt/TiO₂(H₂PtCl₆), Ba-Pt/TiO₂(H₂PtCl₆), Pt/TiO₂(Pt(NH₃)₄(NO₃)₂) and Ba-Pt/TiO₂(Pt(NH₃)₄(NO₃)₂) catalysts.

The chemical valence states of various elements in different catalysts are ascertained by XPS analyses. As illustrated in Figure 4a, the Pt 4f XPS data of four catalysts reveal three doubly occupied states with binding energies of 71.1–74.5 eV, 72.0–75.6 eV and 73.2–76.6 eV, which correspond to the characteristics of Pt⁰, Pt²⁺ and Pt⁴⁺, respectively [36,37]. Based on the signal intensity, the proportions of the various Pt species of the catalysts are calculated with the results listed in Table S2. Obviously, four catalysts have the similar proportions of metallic Pt. However, the proportions of Pt²⁺ species in each catalyst are as follows: 28% for Pt/TiO₂(H₂PtCl₆), 30% for Ba-Pt/TiO₂(H₂PtCl₆), 29% for Pt/TiO₂(Pt(NH₃)₄(NO₃)₂), and 41% for Ba-Pt/TiO₂(Pt(NH₃)₄(NO₃)₂). Herein, the dramatically highest proportion of Pt²⁺ species is observed on Ba-Pt/TiO₂(Pt(NH₃)₄(NO₃)₂), which further evidences the formation of the Ba-O-Pt active site [7]. This finding is also consistent with the CO-DRIFTS results mentioned above.

Figure 4b shows the Ba 3d XPS data of Ba/TiO₂, Ba-Pt/TiO₂(H₂PtCl₆), and Ba-Pt/TiO₂(Pt(NH₃)₄(NO₃)₂) samples. The binding energies of Ba 3d are observed at 794.6 eV and 779.1 eV, ascribed to the Ba 3d_{3/2} and Ba 3d_{5/2} orbitals, respectively [38]. It is noteworthy that the Ba 3d_{5/2} peak in both Ba/TiO₂ and Ba-Pt/TiO₂(H₂PtCl₆) samples is centered at 779.1 eV, which indicates the same state of the Ba species in two catalysts. In contrast, the Ba 3d_{5/2} peak in Ba-Pt/TiO₂(Pt(NH₃)₄(NO₃)₂) exhibits a significant shift towards the high binding energy, with its peak located at 780.0 eV. This shift suggests a reduction in the electron density of Ba element in Ba-Pt/TiO₂(Pt(NH₃)₄(NO₃)₂). Specifically, electrons transfer from Ba²⁺ to the Pt species, leading to an accumulation of electrons on Pt nanoparticles. This phenomenon elucidates why the Ba-Pt/TiO₂(Pt(NH₃)₄(NO₃)₂) catalyst exhibits a higher proportion of Pt²⁺ compared to other catalysts, even though they possess a similar content of Pt⁰. The current findings further support previous assertions regarding the formation of the Ba-O-Pt active site. Moreover, the Ti 2p XPS data of four catalysts are presented in Figure 4c. The binding energies of Ti 2p are observed at 758.4 eV and 464.1 eV, corresponding to the Ti 2p_{3/2} and Ti 2p_{1/2} orbitals of Ti⁴⁺ species, respectively [34,39]. Notably, the binding energy of Ti 2p across all four catalysts aligns along a single straight line without

any obvious shift, further indicating that the interaction occurs primarily between Pt and Ba, which is independent of the TiO₂ support.

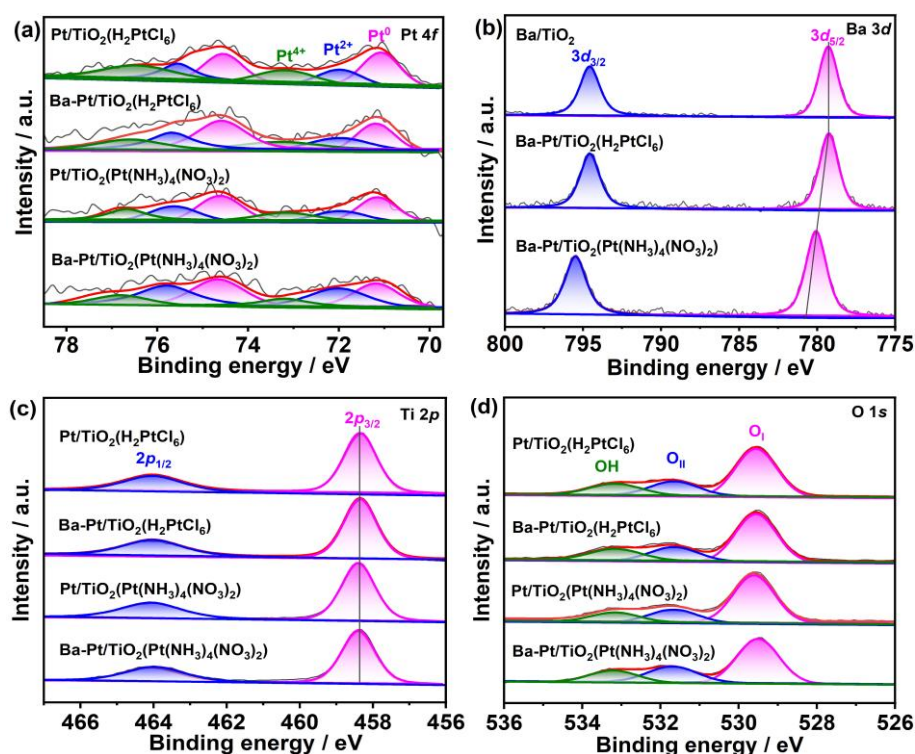


Figure 4. XPS data for Pt 4f (a), Ba 3d (b), Ti 2p (c) and O 1s (d) of Pt/TiO₂(H₂PtCl₆), Ba-Pt/TiO₂(H₂PtCl₆), Pt/TiO₂(Pt(NH₃)₄(NO₃)₂), Ba-Pt/TiO₂(Pt(NH₃)₄(NO₃)₂) and Ba/TiO₂ samples.

3.3. Active Site Formation Mechanism Analysis

It has been confirmed the formation of the Ba-O-Pt active site in the Ba-Pt/TiO₂(Pt(NH₃)₄(NO₃)₂) catalyst in the preceding section. To further elucidate the formation mechanism of such site, the structure of Pt/TiO₂(Pt(NH₃)₄(NO₃)₂) at different preparation stages are detailly analyzed. Firstly, the reduction process of various catalysts is characterized using H₂-TPR. As illustrated in Figure 5a, all samples exhibit a profile that can be divided into two distinct regions: low temperature (<200 °C) and high temperature (>200 °C), which correspond to the reduction of the oxidized Pt and Ba species, respectively [22]. The temperatures of the first reduction peak exhibit a notable similarity across all four catalysts, occurring at approximately 15 °C. For Ba-Pt/TiO₂(Pt(NH₃)₄(NO₃)₂) and Ba-Pt/TiO₂(H₂PtCl₆) samples, two distinct peaks of H₂ consumption are observed in their H₂-TPR profiles. Note that the reduction temperatures of the oxidized Ba species in both Ba-Pt/TiO₂(Pt(NH₃)₄(NO₃)₂) and Ba-Pt/TiO₂(H₂PtCl₆) samples significantly decrease to 354.5 and 450.3 °C, respectively, which can be attributed to the activation of H₂ by metallic Pt [22]. Moreover, the H₂ consumption amount of the first reduction peak of various catalysts was calculated by a normalization method and summarized in Table S1. It can be seen that the H₂ consumption amount of Ba-Pt/TiO₂(Pt(NH₃)₄(NO₃)₂) (2.52) is 2.6 times larger than that of Pt/TiO₂(Pt(NH₃)₄(NO₃)₂) (0.97). Apparently, a part of the oxidized Ba species is reduced with the reduction of the oxidized Pt species in Ba-Pt/TiO₂(Pt(NH₃)₄(NO₃)₂), suggesting the presence of the interaction between the oxidized Pt and Ba species. In contrast, the H₂ consumption amount of the first reduction peak of Ba-Pt/TiO₂(H₂PtCl₆) (1.28) compared with that of Pt/TiO₂(H₂PtCl₆) (1.0) does not increase significantly. It demonstrates that the Pt-Ba interaction is limited in the Ba-mediated Pt/TiO₂ catalyst when H₂PtCl₆ is used as the Pt precursor. This result indicates that the oxidized Ba species can strongly interact with the oxidized Pt species prior to the reduction of the Pt/TiO₂(Pt(NH₃)₄(NO₃)₂) catalyst.

The chemical valences of various elements at the impregnation stage are further characterized to analyze the influence of the dispersion state of precursors on the formation of the active site. As illustrated in Figure S3a, the Pt 4f XPS data indicate that the Pt/TiO₂(H₂PtCl₆)-impregnated sample contains both Pt⁴⁺ and a minor amount of Pt²⁺. Theoretically, Pt in H₂PtCl₆ is expected to exist solely as Pt⁴⁺. The presence of Pt²⁺ in the impregnated sample may be attributed to the interaction between H₂PtCl₆ and TiO₂ or to the partial reduction induced by Ar⁺ ion bombardment before XPS analysis [40]. However, following the introduction of Ba(NO₃)₂, the valent state of Pt in the Ba-Pt/TiO₂(H₂PtCl₆)-impregnated remains largely unchanged, suggesting that no significant interaction

occurs between $\text{Ba}(\text{NO}_3)_2$ and H_2PtCl_6 during the impregnation process. This conclusion is further supported by the analysis of $\text{Cl } 2p$ (Figure S3b) and $\text{Ba } 3d$ (Figure S3c) XPS data. For the $\text{Pt}/\text{TiO}_2(\text{Pt}(\text{NH}_3)_4(\text{NO}_3)_2)$ -impregnated sample, signals corresponding to both Pt^{4+} and Pt^{2+} species are observed in the XPS result. Considering that Pt from $\text{Pt}(\text{NH}_3)_4(\text{NO}_3)_2$ should exist in a divalent ionic state, the detection of Pt^{4+} signal suggests that this precursor undergoes decomposition during the impregnation process. This observation is corroborated by $\text{N } 1s$ XPS data (Figure S3d), which reveals a disappearance of NO_3^- signal alongside retention of NH_3^- signal [41,42]. After introducing $\text{Ba}(\text{NO}_3)_2$, there is only a slight change in Pt signal within the $\text{Ba-Pt}/\text{TiO}_2(\text{Pt}(\text{NH}_3)_4(\text{NO}_3)_2)$ -impregnated sample. Notably, there is no high-binding-energy shift for the $\text{Ba } 3d_{5/2}$ peak in the $\text{Ba-Pt}/\text{TiO}_2(\text{Pt}(\text{NH}_3)_4(\text{NO}_3)_2)$ -impregnated sample, indicating the establishment of such strong interaction between Ba and Pt requires the subsequent high-temperature calcination.

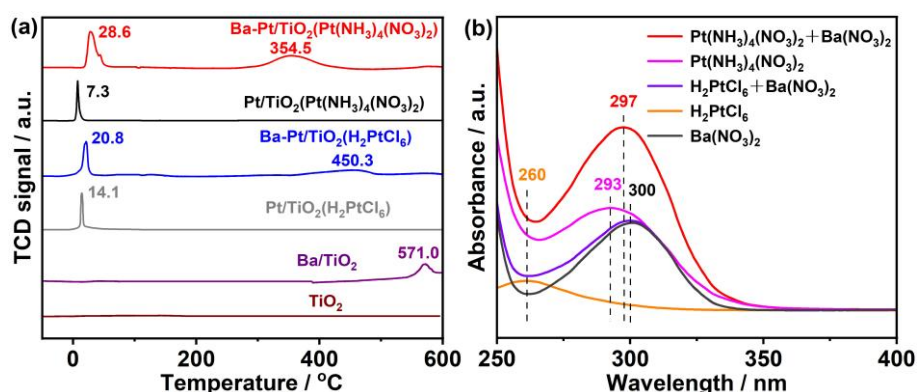


Figure 5. H_2 -TPR profiles of various calcined catalysts (a), UV-Vis spectra of different impregnation solutions (b).

To investigate whether the co-impregnation of $\text{Ba}(\text{NO}_3)_2$ and Pt precursors influences the formation of the active site, an analysis of the precursor state during the impregnation solution stage is conducted. As illustrated in Figure 5b, the UV-Vis absorption spectrum of H_2PtCl_6 solution exhibits a characteristic peak at 260 nm, which is attributed to the $[\text{PtCl}_6]^{2-}$ anionic complex [43]. In contrast, for the $\text{Pt}(\text{NH}_3)_4(\text{NO}_3)_2$ solution, an absorption band at 293 nm is observed which are common to the structure of square-planar Pt complexes [44]. The $\text{Ba}(\text{NO}_3)_2$ solution displays a signal peak at 300 nm, associated with the characteristics of barium ion [45]. Upon mixing $\text{Ba}(\text{NO}_3)_2$ with H_2PtCl_6 , there is no change in the position of this signal peak, indicating there is no interaction between $\text{Ba}(\text{NO}_3)_2$ and H_2PtCl_6 in the impregnation solution. It also aligns with the XPS result from the impregnated samples. Notably, when $\text{Pt}(\text{NH}_3)_4(\text{NO}_3)_2$ is mixed with $\text{Ba}(\text{NO}_3)_2$, a shift in the signal peak to 297 nm is observed in the UV-vis spectrum of their mixed solution, which indicates an interaction between $\text{Pt}(\text{NH}_3)_4(\text{NO}_3)_2$ and $\text{Ba}(\text{NO}_3)_2$. Consequently, it can be determined that the formation of the Ba-O-Pt active site in the $\text{Ba-Pt}/\text{TiO}_2(\text{Pt}(\text{NH}_3)_4(\text{NO}_3)_2)$ catalyst is closely associated with the interaction between the Pt and Ba species occurring at various stages of preparation.

3.4. Structure-Performance Relationship Analysis

Based on the above results, it can be concluded that the Ba-O-Pt active site is formed in the $\text{Ba-Pt}/\text{TiO}_2(\text{Pt}(\text{NH}_3)_4(\text{NO}_3)_2)$ catalyst, which shows superior performance in HCHO oxidation. Subsequently, the relationship between the Ba-O-Pt active site and the HCHO oxidation performance is investigated to elucidate the promotion roles of Ba as a promoter.

For the oxidation reactions, the activation of oxygen species on the catalyst is crucial to obtaining efficient catalytic performance. The adsorbed state of oxygen species on the catalyst is analyzed through O_2 -TPD, and the corresponding results are displayed in Figure 6. Within the temperature range of 0~600 °C, all catalysts exhibit a broad O_2 desorption peak. For $\text{Pt}/\text{TiO}_2(\text{H}_2\text{PtCl}_6)$, $\text{Ba-Pt}/\text{TiO}_2(\text{H}_2\text{PtCl}_6)$ and $\text{Pt}/\text{TiO}_2(\text{Pt}(\text{NH}_3)_4(\text{NO}_3)_2)$, the peak values for O_2 desorption temperature are similar, which are observed at 251.3 °C, 248.0 °C, and 234.1 °C, respectively. In contrast, the O_2 desorption peak of $\text{Ba-Pt}/\text{TiO}_2(\text{Pt}(\text{NH}_3)_4(\text{NO}_3)_2)$ catalyst illustrates a shift to a lower temperature, reaching its maximum at 188.5 °C. It suggests that O_2 adsorbed on $\text{Ba-Pt}/\text{TiO}_2(\text{Pt}(\text{NH}_3)_4(\text{NO}_3)_2)$ are liable to be activated at a lower temperature than those on the other three catalysts [22]. Additionally, there is an increase in the area of the O_2 desorption peak of $\text{Ba-Pt}/\text{TiO}_2(\text{Pt}(\text{NH}_3)_4(\text{NO}_3)_2)$ compared to those of other catalysts, which indicates that $\text{Ba-Pt}/\text{TiO}_2(\text{Pt}(\text{NH}_3)_4(\text{NO}_3)_2)$ can adsorb a higher amount of O_2 . Both factors are essential for the development of highly efficient low temperature HCHO oxidation catalysts.

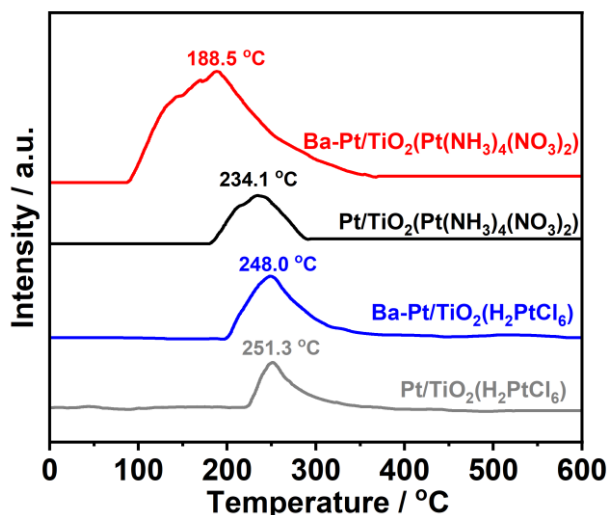


Figure 6. O₂-TPD patterns of Pt/TiO₂(H₂PtCl₆), Ba-Pt/TiO₂(H₂PtCl₆), Pt/TiO₂(Pt(NH₃)₄(NO₃)₂) and Ba-Pt/TiO₂(Pt(NH₃)₄(NO₃)₂) catalysts.

Furthermore, the type of the oxygen species on various catalysts is identified by O 1s XPS analyses. Figure 4d presents the asymmetric O 1s XPS data of four catalysts, which can be deconvoluted into three distinct peaks. The binding energy corresponding to the bulk TiO₂ lattice oxygen (O_I) is measured at 529.7 eV. Surface oxygen (O_{II}) and surface hydroxyl (OH) oxygen are identified at binding energies ranging from 1.1 eV to 1.3 eV and from 2.1 eV to 2.3 eV above that of the O_I, respectively [46,47]. Among them, O_{II} and OH species are considered to participate in the catalytic oxidation of HCHO [7,27]. From Table S2, it is evident that the O_{II}/O_I (0.43) and OH/O_I (0.31) values for the Ba-Pt/TiO₂(Pt(NH₃)₄(NO₃)₂) catalyst are the highest among those samples. This further substantiates that more active oxygen species can be generated on Ba-Pt/TiO₂(Pt(NH₃)₄(NO₃)₂) due to the presence of the Ba-O-Pt active site, as also consistent with the O₂-TPD analyses.

After clarifying the characteristics of oxygen species, investigation in the reaction mechanism of HCHO oxidation over four catalysts is further conducted through the HCHO-DRIFTS experiment, and the corresponding results are shown in Figure S5. Figure 7a,c illustrate that, after exposure to an atmosphere of HCHO + H₂O + N₂ for 60 min, the Pt/TiO₂(H₂PtCl₆) and Pt/TiO₂(Pt(NH₃)₄(NO₃)₂) catalysts exhibit formate species (HCOO⁻) in the DRIFT spectra, which is evidenced by $\nu(\text{HCOO}^-)$ at 1570 cm⁻¹, 1360 cm⁻¹, and $\nu(\text{C-H})$ at 2860 cm⁻¹. Following a N₂ purge for an additional 60 min, the formate species is decomposed into CO species (ca. 2060 cm⁻¹). Upon exposure to O₂, the CO species is subsequently converted to CO₂ and desorbs from the catalyst surface. Thus, the oxidation reaction of HCHO over the Pt/TiO₂(H₂PtCl₆) and Pt/TiO₂(Pt(NH₃)₄(NO₃)₂) catalysts proceeds via a pathway, i.e., HCHO → HCOO⁻ → CO → CO₂, which has been generally reported in the literatures [48,49]. The conversion of formate to CO represents the rate-determining step of HCHO oxidation due to the obvious signal of formate. Notably, for the Ba-Pt/TiO₂(H₂PtCl₆) catalyst (Figure 7b), the same reaction pathway of HCHO oxidation is also applicable. It illustrates why Ba-Pt/TiO₂(H₂PtCl₆) and Pt/TiO₂(H₂PtCl₆) have the comparable HCHO oxidation performance.

In regard to the Ba-Pt/TiO₂(Pt(NH₃)₄(NO₃)₂) catalyst (Figure 7d), after 60 min of reaction in HCHO + H₂O + O₂, the formation of formate ($\nu(\text{HCOO}^-)$ at 1590 cm⁻¹ and 1340 cm⁻¹, $\nu(\text{C-H})$ at 2860 cm⁻¹) predominates on the catalyst surface [50]. Note that following N₂ purification, both the peak intensities of HCOO⁻ and OH bands decrease simultaneously, with almost no formate species detected. Concurrently, peaks associated with surface carbonates and bicarbonates (1310 cm⁻¹ and 1550 cm⁻¹) emerge and increase as the formate species are consumed. Further purging with O₂ reveals no significant spectral change, indicating an absence of additional reactions. The additional evidence is provided in Figure S6, which shows that there is no obvious change in the signal intensities of formate and CO in the DRIFT spectra of Ba-Pt/TiO₂(Pt(NH₃)₄(NO₃)₂) catalyst during the N₂ purging stage after 60 min. Obviously, the HCHO oxidation is carried out on Ba-Pt/TiO₂(Pt(NH₃)₄(NO₃)₂) via the same reaction pathway (HCHO → HCOO⁻ + OH → H₂O + CO₂) to that observed in alkali-mediated Pt/TiO₂ system [7,51]. This serves as an evidence for the absence of formate signal. On the Ba-O-Pt active site of Pt/TiO₂(Pt(NH₃)₄(NO₃)₂), the formate species can be liable to react with active OH groups to yield carbonates or bicarbonates, which avoids the conventional issue of the formate accumulation on the catalysts [7,50]. It explains why Ba-Pt/TiO₂(Pt(NH₃)₄(NO₃)₂) exhibits higher TOF and lower *E_a* values than those of the other three catalysts.

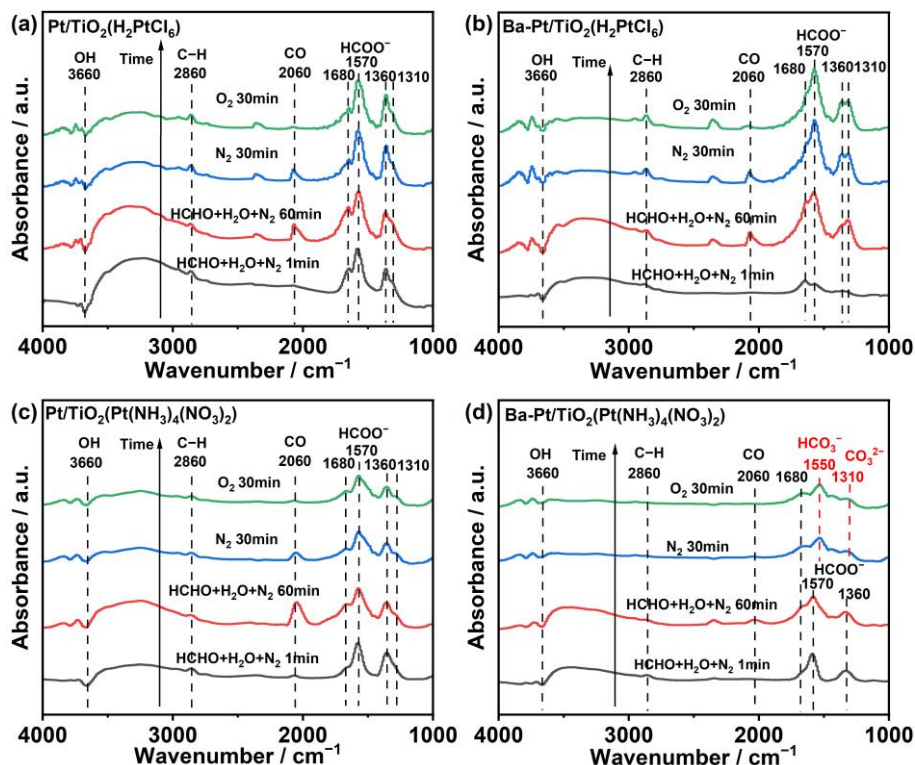


Figure 7. Representative HCHO-DRIFT spectra of Pt/TiO₂(H₂PtCl₆) (a), Ba-Pt/TiO₂(H₂PtCl₆) (b), Pt/TiO₂(Pt(NH₃)₄(NO₃)₂) (c) and Ba-Pt/TiO₂(Pt(NH₃)₄(NO₃)₂) (d) with a flow of HCHO + H₂O + N₂ for 60 min, N₂ purging for 30 min, and finally O₂ purging for 30 min.

Based on the above analyses, the reaction mechanism involving different Pt precursors and a Ba promoter on various Pt/TiO₂ catalysts for HCHO oxidation is proposed, as illustrated in Figure 8. The Pt/TiO₂ catalyst, irrespective of whether H₂PtCl₆ or Pt(NH₃)₄(NO₃)₂ is employed as a Pt precursor, adheres to the conventional reaction pathway for HCHO oxidation (HCHO → HCOO⁻ → CO → CO₂). Upon introducing Ba(NO₃)₂ into H₂PtCl₆, no strong interaction between Ba and Pt species is observed, which results in the Pt/TiO₂(H₂PtCl₆) catalyst exhibiting a similar catalytic performance to those of Pt/TiO₂ catalysts by following the same reaction pathway. Conversely, when using Pt(NH₃)₄(NO₃)₂ as the precursor alongside the Ba promoter, a strong interaction between Ba and Pt leads to form the Ba-O-Pt active site. On such Ba-Pt/TiO₂(Pt(NH₃)₄(NO₃)₂) catalyst, more reactive oxygen species and hydroxyl groups are adsorbed and activated to engage in the oxidation of HCHO through a different but efficient reaction pathway (HCHO → HCOO⁻ + OH → H₂O + CO₂), thereby enhancing the catalytic activity of HCHO oxidation.

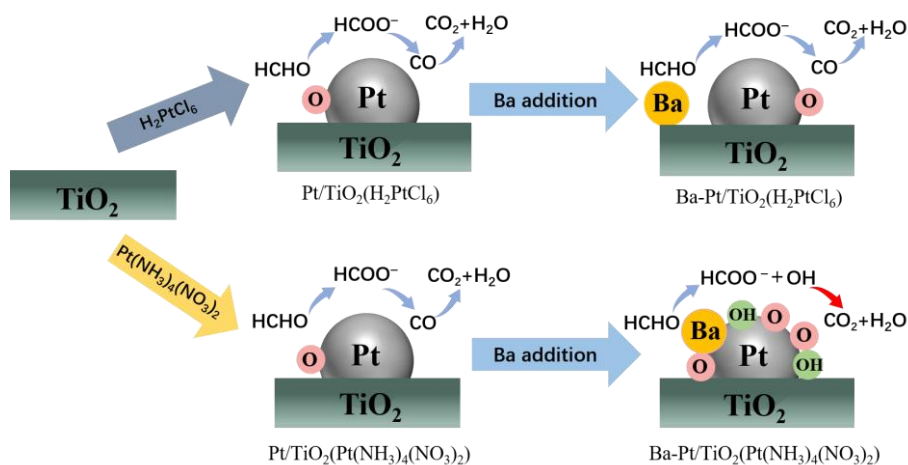


Figure 8. Scheme for the catalytic oxidation of HCHO on Pt/TiO₂(H₂PtCl₆), Ba-Pt/TiO₂(H₂PtCl₆), Pt/TiO₂(Pt(NH₃)₄(NO₃)₂) and Ba-Pt/TiO₂(Pt(NH₃)₄(NO₃)₂) catalysts.

4. Conclusions

To sum up, the Pt precursor has been demonstrated to play a critical role in achieving highly efficient Ba-mediated Pt/TiO₂ catalyst. Structural characterization results revealed that due to the presence of a strong interaction between the Ba and Pt species derived from the Pt(NH₃)₄(NO₃)₂ precursor, the Ba-O-Pt active site can be formed. In contrast, when using H₂PtCl₆ precursor, such interaction was absent in the Ba-mediated Pt/TiO₂ catalyst, resulting in its catalytic and structural characteristics similar to those of Pt/TiO₂. Detailed analysis showed that Ba-Pt/TiO₂(Pt(NH₃)₄(NO₃)₂) had an increased ability to adsorb and activate more oxygen species and hydroxyl groups for efficiently oxidizing HCHO via an alternative reaction pathway. This work highlights the importance of Pt precursor in developing Ba-mediated catalysts for efficient HCHO oxidation, and elucidates the roles of the effective activity site together with its reaction mechanism, both of which can facilitate the development of efficient alkali metal-mediated catalysts.

Supplementary Materials: The following supporting information can be downloaded at: <https://www.sciltp.com/journals/see/2025/1/612/s1>. Figure S1: XRD patterns of Pt/TiO₂(H₂PtCl₆), Ba-Pt/TiO₂(H₂PtCl₆), Pt/TiO₂(Pt(NH₃)₄(NO₃)₂) and Ba-Pt/TiO₂(Pt(NH₃)₄(NO₃)₂); Figure S2: N₂ adsorption/desorption isotherms of Pt/TiO₂(H₂PtCl₆), Ba-Pt/TiO₂(H₂PtCl₆), Pt/TiO₂(Pt(NH₃)₄(NO₃)₂) and Ba-Pt/TiO₂(Pt(NH₃)₄(NO₃)₂). Inserted diagram shows the pore size distribution curves of four samples; Figure S3: XPS spectra for Pt 4f (c), Cl 2p (d), Ba 3d (e), N 1s (f) of various impregnated samples; Figure S4: The dynamic CO adsorption *in situ* DRIFTS of Pt/TiO₂(H₂PtCl₆) (a), Ba-Pt/TiO₂(H₂PtCl₆) (b), Pt/TiO₂(Pt(NH₃)₄(NO₃)₂) (c) and Ba-Pt/TiO₂(Pt(NH₃)₄(NO₃)₂) (d) catalysts with N₂ purge; Figure S5: HCHO-DRIFTS spectra of Pt/TiO₂(H₂PtCl₆) (a), Ba-Pt/TiO₂(H₂PtCl₆) (b), Pt/TiO₂(Pt(NH₃)₄(NO₃)₂) (c) and Ba-Pt/TiO₂(Pt(NH₃)₄(NO₃)₂) (d) with a flow of HCHO+H₂O+N₂ for 60 min, N₂ purging for 30 min, and finally O₂ purging for 30 min; Figure S6: The band intensities of formate (a) and CO (b) as a function of time for Pt/TiO₂(H₂PtCl₆), Ba-Pt/TiO₂(H₂PtCl₆), Pt/TiO₂(Pt(NH₃)₄(NO₃)₂) and Ba-Pt/TiO₂(Pt(NH₃)₄(NO₃)₂); Table S1: Physicochemical properties of various catalysts; Table S2: Summarized XPS data of various catalysts, and equations for TOF calculations along with the dispersion of Pt nanoparticles.

Author Contributions: Conceptualization, S.C. and L.L.; validation, C.R., H.G., Z.H. and S.L.; resources, X.Z. and L.L.; data curation, C.R., Z.H. and S.L.; writing—original draft preparation, C.R.; writing—review and editing, S.C. and L.L.; supervision, X.Z. and S.C. and L.L. All authors have read and agreed to the published version of the manuscript.

Funding: This research was funded by the general program of National Natural Science Foundation of China (22272082 and 21978134).

Institutional Review Board Statement: Not applicable.

Informed Consent Statement: Not applicable.

Data Availability Statement: Not applicable.

Conflicts of Interest: The authors declare that they have no known competing financial interests or personal relationships that could have appeared to influence the work reported in the present paper.

References

1. Guo, J.; Lin, C.; Jiang, C.; Zhang, P. Review on noble metal-based catalysts for formaldehyde oxidation at room temperature. *Appl. Surf. Sci.* **2019**, *475*, 237–255.
2. Miao, L.; Wang, J.; Zhang, P. Review on manganese dioxide for catalytic oxidation of airborne formaldehyde. *Appl. Surf. Sci.* **2019**, *466*, 441–453.
3. Zhang, Z.; He, G.; Li, Y.; Zhang, C.; Ma, J.; He, H. Effect of hydroxyl groups on metal anchoring and formaldehyde oxidation performance of Pt/Al₂O₃. *Environ. Sci. Technol.* **2022**, *56*, 10916–10924.
4. Ahmad, W.; Jeong, H.; Nahm, H.; Lee, Y.; Park, E.; Lee, H.; Ali, G.; Kim, Y.; Jurng, J.; Oh, Y. Metal-anchoring, metal oxidation-resistance, and electron transfer behavior of oxygen vacancy-rich TiO₂ in supported noble metal catalyst for room temperature HCHO conversion. *Chem. Eng. J.* **2023**, *467*, 143412.
5. Wang, C.; Li, Y.; Zheng, L.; Zhang, C.; Wang, Y.; Shan, W.; Liu, F.; He, H. A nonoxide catalyst system study: Alkali metal-promoted Pt/AC catalyst for formaldehyde oxidation at ambient temperature. *ACS Catal.* **2020**, *11*, 456–465.
6. Chen, D.; Zhang, G.; Wang, M.; Li, N.; Xu, Q.; Li, H.; He, J.; Lu, J. Pt/MnO₂ nanoflowers anchored to boron nitride aerogels for highly efficient enrichment and catalytic oxidation of formaldehyde at room temperature. *Angew. Chem. Int. Ed.* **2021**, *60*, 6377–6381.
7. Zhang, C.; Liu, F.; Zhai, Y.; Ariga, H.; Yi, N.; Liu, Y.; Asakura, K.; Flytzani-Stephanopoulos, M.; He, H. Alkali-metal-promoted Pt/TiO₂ opens a more efficient pathway to formaldehyde oxidation at ambient temperatures. *Angew. Chem. Int. Ed.* **2012**, *51*, 9628–9632.
8. Li, Y.; Zhang, C.; He, H.; Zhang, J.; Chen, M. Influence of alkali metals on Pd/TiO₂ catalysts for catalytic oxidation of formaldehyde at room temperature. *Catal. Sci. Technol.* **2016**, *6*, 2289–2295.
9. Wang, J.; He, G.; Wang, C.; Chen, X.; Liu, X.; Li, Y.; Shan, W.; He, H. HCHO oxidation on Pt-Na/SiO₂ catalyst with ultralow Pt loading: New insight into the effect of Si support and Na promoter. *Appl. Catal. B Environ.* **2024**, *347*, 123787.

10. Zhao, H.; Tang, B.; Tang, J.; Cai, Y.; Cui, Y.; Liu, H.; Wang, L.; Wang, Y.; Zhan, W.; Guo, Y. et al. Ambient temperature formaldehyde oxidation on the Pt/Na-ZSM-5 catalyst: Tuning adsorption capacity and the Pt chemical state. *Ind. Eng. Chem. Res.* **2021**, *60*, 7132–7144.
11. Xiang, N.; Hou, Y.; Han, X.; Li, Y.; Guo, Y.; Liu, Y.; Huang, Z. Promoting effect and mechanism of alkali Na on Pd/SBA-15 for room temperature formaldehyde catalytic oxidation. *ChemCatChem* **2019**, *11*, 5098–5107.
12. Panagiotopoulou, P.; Kondarides, D. Effects of promotion of TiO₂ with alkaline earth metals on the chemisorptive properties and water–gas shift activity of supported platinum catalysts. *Appl. Catal. B Environ.* **2011**, *101*, 738–746.
13. Bauer, H.; Thum, K.; Alonso, M.; Fischer, C.; Harder, S. Alkene transfer hydrogenation with alkaline-earth metal catalysts. *Angew. Chem. Int. Ed.* **2019**, *58*, 4248–4253.
14. Fan, J.; Chen, L.; Li, S.; Mou, J.; Zeng, L.; Jiao, Y.; Wang, J.; Chen, Y. Insights into the promotional effect of alkaline earth metals in Pt-based three-way catalysts for NO reduction. *J. Catal.* **2023**, *418*, 90–99.
15. Auvray, X.; Lindholm, A.; Milh, M.; Olsson, L. The addition of alkali and alkaline earth metals to Pd/Al₂O₃ to promote methane combustion. Effect of Pd and Ca loading. *Catal. Today* **2018**, *299*, 212–218.
16. Zhang, Z.; Ou, Z.; Qin, C.; Ran, J.; Wu, C. Roles of alkali/alkaline earth metals in steam reforming of biomass tar for hydrogen production over perovskite supported Ni catalysts. *Fuel* **2019**, *257*, 116032.
17. Xu, A.; Hung, S.; Cao, A.; Wang, Z.; Karmodak, N.; Huang, J.; Yan, Y.; Sedighian Rasouli, A.; Ozden, A.; Wu, F. Copper/alkaline earth metal oxide interfaces for electrochemical CO₂-to-alcohol conversion by selective hydrogenation. *Nat. Catal.* **2022**, *5*, 1081–1088.
18. Mai, J.; Maurer, J.; Langer, J.; Harder, S. Heterobimetallic alkaline earth metal–metal bonding. *Nat. Synth.* **2024**, *3*, 368–377.
19. Liu, K.; Xu, X.; Xu, J.; Fang, X.; Liu, L.; Wang, X. The distributions of alkaline earth metal oxides and their promotional effects on Ni/CeO₂ for CO₂ methanation. *J. CO₂ Util.* **2020**, *38*, 113–124.
20. Solís, R.; Bedia, J.; Rodríguez, J.; Belver, C. A review on alkaline earth metal titanates for applications in photocatalytic water purification. *Chem. Eng. J.* **2021**, *409*, 128110.
21. Zhai, Y.; Pierre, D.; Si, R.; Deng, W.; Ferrin, P.; Nilekar, A.; Peng, G.; Herron, J.; Bell, D.; Saltsburg, H. et al. Alkali-stabilized Pt-OH_x species catalyze low-temperature water-gas shift reactions. *Science* **2010**, *329*, 1633–1636.
22. Chen, X.; Qin, Q.; Wang, J.; Wen, W.; Liu, X.; Wang, C.; Zhou, L.; Deng, H.; Li, Y. Strong interaction between promoter and metal in Pd-Ba/TiO₂ catalysts for formaldehyde oxidation. *J. Colloid Interf. Sci.* **2025**, *678*, 520–531.
23. Huang, H.; Leung, D. Complete elimination of indoor formaldehyde over supported Pt catalysts with extremely low Pt content at ambient temperature. *J. Catal.* **2011**, *280*, 60–67.
24. Li, L.; Li, L.; Wang, L.; Zhao, X.; Hua, Z.; Chen, Y.; Li, X.; Gu, X. Enhanced catalytic decomposition of formaldehyde in low temperature and dry environment over silicate-decorated titania supported sodium-stabilized platinum catalyst. *Appl. Catal. B Environ.* **2020**, *277*, 119–216.
25. Zhao, H.; Tang, J.; Li, Z.; Yang, J.; Liu, H.; Wang, L.; Cui, Y.; Zhan, W.; Guo, Y.; Guo, Y. Nickel oxide regulating surface oxygen to promote formaldehyde oxidation on manganese oxide catalysts. *Catal. Sci. Technol.* **2021**, *11*, 7110–7124.
26. Bu, Y.; Chen, Y.; Jiang, G.; Hou, X.; Li, S.; Zhang, Z. Understanding of Au-CeO₂ interface and its role in catalytic oxidation of formaldehyde. *Appl. Catal. B Environ.* **2020**, *260*, 118138.
27. Wang, L.; Yue, H.; Hua, Z.; Wang, H.; Li, X.; Li, L. Highly active Pt/Na_xTiO₂ catalyst for low temperature formaldehyde decomposition. *Appl. Catal. B Environ.* **2017**, *219*, 301–313.
28. Li, Y.; Zhang, C.; He, H. Significant enhancement in activity of Pd/TiO₂ catalyst for formaldehyde oxidation by Na addition. *Catal. Today* **2017**, *281*, 412–417.
29. Bai, B.; Li, J. Positive effects of K⁺ ions on three-dimensional mesoporous Ag/Co₃O₄ catalyst for HCHO oxidation. *ACS Catal.* **2014**, *4*, 2753–2762.
30. Song, S.; Wu, X.; Lu, C.; Wen, M.; Le, Z.; Jiang, S. Solid strong base K-Pt/NaY zeolite nano-catalytic system for completed elimination of formaldehyde at room temperature. *Appl. Surf. Sci.* **2018**, *422*, 195–203.
31. Lv, S.; Hua, Z.; Ma, N.; Guo, Z.; Shi, K.; Wei, T.; Li, L.; Li, L. High-pressure steam treatment with Pt/TiO₂ enhances the low temperature formaldehyde oxidation performance. *Appl. Surf. Sci.* **2023**, *620*, 156815.
32. Ohwada, K.; Machida, A. Observation of ferroelectric domains in BaTiO₃ by synchrotron radiation X-ray diffraction topography. *Jpn. J. Appl. Phys.* **2024**, *63*, 09SP15.
33. Bazeera, A.; Amrin, M. Synthesis and characterization of barium oxide nanoparticles. *IOSR J. Appl. Phys.* **2017**, *1*, 76–80.
34. Wei, T.; Zhao, X.; Li, L.; Wang, L.; Lv, S.; Gao, L.; Yuan, G.; Li, L. Enhanced formaldehyde oxidation performance of the mesoporous TiO₂(B)-supported Pt catalyst: The role of hydroxyls. *ACS Omega* **2022**, *7*, 25491–25501.
35. Zeinalipour-Yazdi, C.; Cooksy, A.; Efstathiou, A. CO adsorption on transition metal clusters: Trends from density functional theory. *Surf. Sci.* **2008**, *602*, 1858–1862.

36. Motin, A.; Haunold, T.; Bukhtiyarov, A.; Bera, A.; Rameshan, C.; Rupprechter, G. Surface science approach to Pt/carbon model catalysts: XPS, STM and microreactor studies. *Appl. Surf. Sci.* **2018**, *440*, 680–687.
37. Vovk, E.; Kalinkin, A.; Smirnov, M.; Klembovskii, I.; Bukhtiyarov, V. XPS study of stability and reactivity of oxidized Pt nanoparticles supported on TiO₂. *J. Phys. Chem. C* **2017**, *121*, 17297–17304.
38. Pandian, S.; Sivakumar, M.; Kandasamy, M.; Suresh, S.; Latha, G.; Srinivasan, S.; Ananth, K. Barium titanate nanorods/nanoparticles embedded reduced graphene oxide nanocomposite photoanode for dye-sensitized solar cell. *Chem. Phys. Lett.* **2024**, *851*, 141491.
39. Zhang, C.; Li, Y.; Wang, Y.; He, H. Sodium-promoted Pd/TiO₂ for catalytic oxidation of formaldehyde at ambient temperature. *Environ. Sci. Technol.* **2014**, *48*, 5816–5822.
40. Jardim, E.; Rico-Francés, S.; Coloma, F.; Anderson, J.; Silvestre-Albero, J.; Sepúlveda-Escribano, A. Influence of the metal precursor on the catalytic behavior of Pt/Ceria catalysts in the preferential oxidation of CO in the presence of H₂(PROX). *J. Colloid Interf. Sci.* **2015**, *443*, 45–55.
41. Baltrusaitis, J.; Jayaweera, P.; Grassian, V. XPS study of nitrogen dioxide adsorption on metal oxide particle surfaces under different environmental conditions. *Phys. Chem. Chem. Phys.* **2009**, *11*, 8295–8305.
42. Teske, M.; Lange, H.; Wulf, K.; Senz, V.; Grabow, N.; Eickner, T.; Oschatz, S. Chemical characterization of plasma polymerized allylamine coatings with addition of ammonia and oxygen by XPS. *Curr. Direct. Biomed. Eng.* **2022**, *8*, 664–667.
43. Ueda, Y.; Morisada, S.; Kawakita, H.; Wenzel, M.; Weigand, J.; Ohto, K. Effective extraction of Pt (IV) as [PtCl₆]²⁻ from hydrochloric acid using a simple urea extractant. *Sep. Purif.* **2021**, *277*, 119456.
44. Li, Y.; Hou, Z.; Xiao, Z.; Lu, C.; Jin, J.; He, Y.; Jia, J.; Suntharalingam, K. Modulating the Anticancer Activity of Square-Planar Platinum (II) Complex by Its Chelated Diphosphine. *Appl. Organomet. Chem.* **2025**, *39*, e7803.
45. Ardianrama, A.; Pradyasti, A.; Woo, H.; Kim, M. Colorimetric sensing of barium ion in water based on polyelectrolyte-induced chemical etching of silver nanoprisms. *Dyes Pigm.* **2020**, *181*, 108578.
46. Ruiz-Martínez, J.; Sepúlveda-Escribano, A.; Anderson, J.; Rodríguez-Reinoso, F. Spectroscopic and microcalorimetric study of a TiO₂-supported platinum catalyst. *Phys. Chem. Chem. Phys.* **2009**, *11*, 917–920.
47. He, M.; Ji, J.; Liu, B.; Huang, H. Reduced TiO₂ with tunable oxygen vacancies for catalytic oxidation of formaldehyde at room temperature. *Appl. Surf. Sci.* **2019**, *473*, 934–942.
48. Li, L.; Wang, L.; Zhao, X.; Wei, T.; Wang, H.; Li, X.; Gu, X.; Yan, N.; Li, L.; Xiao, H. Excellent low-temperature formaldehyde decomposition performance over Pt nanoparticles directly loaded on cellulose triacetate. *Ind. Eng. Chem. Res.* **2020**, *59*, 21720–21728.
49. Zhang, C.; He, H.; Tanaka, K. Catalytic performance and mechanism of a Pt/TiO₂ catalyst for the oxidation of formaldehyde at room temperature. *Appl. Catal. B Environ.* **2006**, *65*, 37–43.
50. Li, Y.; Chen, X.; Wang, C.; Zhang, C.; He, H. Sodium enhances Ir/TiO₂ activity for catalytic oxidation of formaldehyde at ambient temperature. *ACS Catal.* **2018**, *8*, 11377–11385.
51. Chen, X.; He, G.; Li, Y.; Chen, M.; Qin, X.; Zhang, C.; He, H. Identification of a facile pathway for dioxymethylene conversion to formate catalyzed by surface hydroxyl on TiO₂-based catalyst. *ACS Catal.* **2020**, *10*, 9706–9715.